

Aberystwyth University

Rapid basal melting of the Greenland Ice Sheet from surface meltwater drainage

Young, Tun Jan; Christoffersen, Poul; Bougamont, Marion; Tulaczyk, Slawek M.; Hubbard, Bryn; Mankoff, Kenneth D.; Nicholls, Keith W.; Stewart, Craig L.

Published in:

Proceedings of the National Academy of Sciences of the United States of America

DOI:

[10.1073/pnas.2116036119](https://doi.org/10.1073/pnas.2116036119)

Publication date:

2022

Citation for published version (APA):

Young, T. J., Christoffersen, P., Bougamont, M., Tulaczyk, S. M., Hubbard, B., Mankoff, K. D., Nicholls, K. W., & Stewart, C. L. (2022). Rapid basal melting of the Greenland Ice Sheet from surface meltwater drainage. *Proceedings of the National Academy of Sciences of the United States of America*, 119(10), [e2116036119]. <https://doi.org/10.1073/pnas.2116036119>

Document License

CC BY

General rights

Copyright and moral rights for the publications made accessible in the Aberystwyth Research Portal (the Institutional Repository) are retained by the authors and/or other copyright owners and it is a condition of accessing publications that users recognise and abide by the legal requirements associated with these rights.

- Users may download and print one copy of any publication from the Aberystwyth Research Portal for the purpose of private study or research.
- You may not further distribute the material or use it for any profit-making activity or commercial gain
- You may freely distribute the URL identifying the publication in the Aberystwyth Research Portal

Take down policy

If you believe that this document breaches copyright please contact us providing details, and we will remove access to the work immediately and investigate your claim.

tel: +44 1970 62 2400

email: is@aber.ac.uk

Rapid basal melting of the Greenland Ice Sheet from surface meltwater drainage

Tun Jan Young^{a,1}, Poul Christoffersen^{a,1,2}, Marion Bougamont^{a,3}, Slawek M. Tulaczyk^b, Bryn Hubbard^c, Kenneth D. Mankoff^d, Keith W. Nicholls^e, and Craig L. Stewart^f

^aScott Polar Research Institute, University of Cambridge, Cambridge CB2 1ER, United Kingdom; ^bEarth & Planetary Sciences, University of California - Santa Cruz, 1156 High Street, Santa Cruz, CA 95064, USA; ^cCentre for Glaciology, Department of Geography and Earth Sciences, Aberystwyth University, Aberystwyth SY23 3DB, United Kingdom; ^dGeological Survey of Denmark and Greenland, Øster Voldgade 10, DK 1350, Copenhagen, Denmark; ^eBritish Antarctic Survey, High Cross, Madingley Road, CB3 0ET, Cambridge, UK; ^fNational Institute for Water and Atmospheric Research, 301 Evans Bay Parade, Greta Point, Wellington, New Zealand

This manuscript was compiled on December 10, 2021

1 **Subglacial hydrologic systems regulate ice sheet flow, causing ac-**
2 **celeration or deceleration depending on hydraulic efficiency and the**
3 **rate at which surface meltwater is delivered to the bed. Because**
4 **these systems are rarely observed, ice sheet basal drainage repre-**
5 **sents a poorly integrated and uncertain component of models used**
6 **to predict sea-level changes. Here, we report radar-derived basal**
7 **melt rates and unexpectedly warm subglacial conditions beneath**
8 **a large Greenlandic outlet glacier. The basal melt rates averaged**
9 **14 mm d⁻¹ over 4 months, peaking at 57 mm d⁻¹ when basal wa-**
10 **ter temperature reached +0.88 °C in a nearby borehole. We attribute**
11 **both observations to the conversion of potential energy of surface**
12 **water as heat in the basal drainage system, which peaked during a**
13 **period of rainfall and intense surface melting. Our findings reveal**
14 **limitations in the theory of channel formation and we show that vis-**
15 **cous dissipation far surpasses other basal heat sources, even in a**
16 **distributed, high-pressure system.**

Greenland | glaciology | ice sheets | hydrology | radio echo sounding

1 **T**he flow of ice sheets and glaciers is controlled by basal
2 motion, which takes place through some combination of
3 hard bed sliding (1–3), sliding induced cavitation (4, 5), and
4 deformation of subglacial sediment (6, 7). All forms of basal
5 motion require a thawed thermal state in order to be substan-
6 tial (8), with more heat produced at (or delivered to) the bed
7 than lost through conduction into the colder ice above (9).
8 Basal motion is also strongly influenced by the way in which
9 hydrologic systems evacuate meltwater (10), which is produced
10 basally as well as at the surface. In settings where surface
11 meltwater is transferred to the bed, drainage is often expected
12 to occur through large channels, which become increasingly
13 efficient in terms of discharge when they grow in size (11, 12).
14 The resulting decrease in water pressure produces arborescent
15 networks in which larger channels capture water from their
16 less efficient surroundings, including smaller channels as well
17 as water stored in small cavities (13), thin films (14) or porous
18 sheets (15). In Greenland, channelized basal drainage has been
19 observed as far as 30 km inland from the land-terminating
20 southwest margin (16) and recent studies show that channels
21 may also form beneath marine-terminating glaciers (17, 18),
22 which drain 88 % of the ice sheet (19). However, the evolution
23 of basal drainage system efficiency, and channels ability to
24 form under thick ice, remain highly uncertain (20, 21).

25 The central process in channel formation is energy dissipa-
26 tion through turbulence and viscous resistance in the water
27 flow, which should make small cavities or sheets unstable (22)
28 and result in channel growth until wall melting balances creep
29 closure (11). In the classic theory of steady-state water flow

in subglacial channels, Röthlisberger (11) assumed that heat
transfer occurs instantaneously and that the temperature of
water is fixed at the pressure-dependent melting temperature
of the ice. Nye (23), followed by Spring and Hutter (24),
extended this theory to consider transient water flow with
temperature dependent heat transfer in Icelandic subglacial
outburst floods (Jökulhlaup) (25). However, with a paucity of
data to confirm how energy is dissipated in basal drainage sys-
tems more broadly, Röthlisberger's simpler theory has become
a cornerstone in hydrologic glacier models today (26).

Here, we report a time series of radar-derived basal melt
rates (BMRs) together with contemporaneous, co-located bore-
hole records showing basal water pressure and temperature of
water beneath a large Greenlandic outlet glacier. The reported
BMR is unprecedented because it is two orders of magnitude
higher than previous estimates for an ice sheet (27, 28) and
comparable to the rate of meltwater generation at the surface.
The high magnitude is corroborated by independent borehole
records, which are the first to capture the temperature depen-
dency of heat transfer and viscous energy dissipation in the
basal drainage system of an ice sheet.

Significance Statement

Subglacial drainage systems control ice sheet flow and the quantity of ice discharged into the ocean. However, these systems are currently poorly characterised from a lack of direct observations. This shortcoming is problematic, as changes in drainage systems can result in a markedly differently ice sheet response. Here, we present a radar-derived record of basal melt rates with co-located borehole observations, showing unexpectedly warm subglacial conditions beneath a large outlet glacier in west Greenland. The record is unprecedented because the observed basal melt rates are several orders of magnitude higher than predictions and previous estimates. Our observations show that the effect of viscous dissipation from surface meltwater input is by far the largest heat source beneath the Greenland Ice Sheet.

TJY and PC designed the experiment with support from KWN. TJY, PC and BH deployed the ApRES system and integrated the co-located borehole data from Store Glacier. PC led the fieldwork and acquired the funding with contributions from BH. TJY processed the ApRES data with support from KWN and CLS. TJY and PC analyzed the radar derived basal melt rates with help from MB, ST and KDM, who contributed to the analysis of subglacial heat transfer. PC and TJY wrote the manuscript with contributions from all co-authors.

The authors declare no competing interests.

²To whom correspondence should be addressed. E-mail: pc350@cam.ac.uk

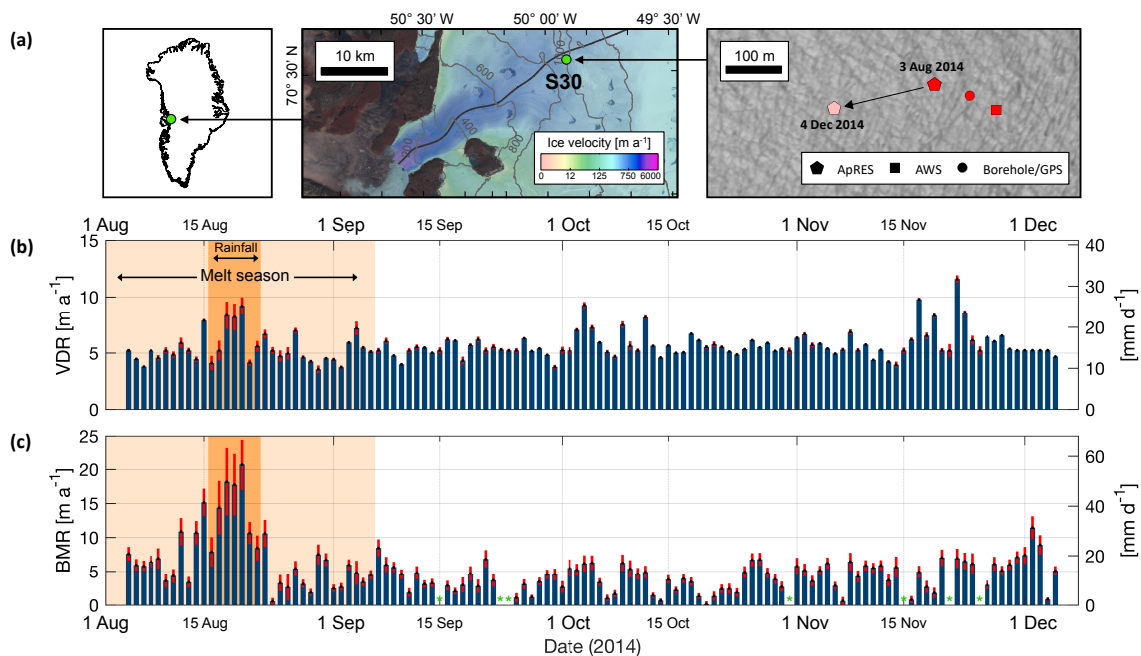


Fig. 1. Vertical ice deformation and basal melt rates observed with radar beneath Store Glacier, Greenland. (a) Location and LandSat-8 image (acquired 1 July 2014) showing Store Glacier and the S30 study site in Greenland. Black line shows the central flowline. (b) Daily vertical deformation rate (VDR) of the ice column at S30 derived by tracking internal layers displacements over time (positive when ice column thickens). Light orange shading highlights periods with surface melt. Dark orange shading shows a cyclonic rainfall event with intensified surface melting due to warm atmospheric conditions. Red bars represent the standard error. (c) Daily basal melt rate (BMR) obtained by subtracting total vertical ice deformation shown in (b) from phase-sensitive measurements of the ice column thickness. Red bars indicate standard error calculated as the square root sum of error terms. Days with insufficient samples (green star) were excluded from the time series.

Results

To quantify basal melting, we used an autonomous phase-sensitive radio-echo sounding (ApRES) instrument, which has millimeter range precision (29), to track the vertical displacement of internal layers and the ice-bed interface of Store Glacier, West Greenland (Methods, Fig. S1). The ApRES instrument was installed 30 km inland from the glacier front, at site S30 (Fig. 1a), where the local ice thickness was estimated to be 604–606 m, and ice properties and basal conditions are well-constrained (30–32). The ApRES instrument was configured to obtain 4-hourly measurements in unattended mode and operated continuously from 3 August to 4 December in 2014.

Radar-derived basal melt rates. Daily BMR was calculated following the same approach used in studies of Antarctic ice shelves (33, 34). In a two-step approach (32), we started by fitting a vertical velocity model to the observed displacement of internal reflectors (Fig. S1). The best fit throughout the entire four month period was a linear regression model (32) (Methods), resulting in positive vertical deformation rates (thickening) averaging $15 \pm 0.7 \text{ mm d}^{-1}$ during the observational period. In the second step, we subtracted the strain-induced thickening from the observed displacement of the ice-bed interface, which was identified clearly at a depth of 604–606 m (Fig. S1). The resulting BMR was positive and persistently high, especially during summer when the average rate was $20 \pm 2.5 \text{ mm d}^{-1}$ (Fig. 1c). We also recorded a distinct peak in basal melting ($57 \pm 10 \text{ mm d}^{-1}$) on 18 August, coincident with high surface melt rates of $56 \text{ mm w.e. d}^{-1}$ during a rainfall event that brought 80 mm of precipitation over six days (Fig. 2). In winter, BMR was notably lower ($9.8 \pm 0.9 \text{ mm d}^{-1}$) and less

variable (Fig. 1c).

Quantifying sources and sinks of heat. The BMR of a grounded ice sheet has not previously been observed or calculated at the precision and daily resolution presented here. We find that the BMR beneath our field location on Store Glacier is two orders of magnitude higher than previous estimates of 0.10 m a^{-1} derived from airborne radio-echo sounding profiles and attributed to high geothermal heat flux in the central Greenland interior (27). To understand why our BMR is so much higher than previous estimates, we quantified the most widely-recognised sources and sinks of basal heat in our study area. As an initial analysis (see breakdown in Methods and Equation 1), we included heat sourced from the geothermal heat flux (0.06 W m^{-2}) and frictional heat ($0.9\text{--}2.6 \text{ W m}^{-2}$, depending on sliding speed and basal shear stress) and an upwards conductive heat loss into the ice base (-0.060 W m^{-2}) (Fig. 3b). Contemporaneous in situ measurements of basal conditions in boreholes drilled to the ice base next to the ApRES (32) enabled all of these contributions to be constrained by direct observations (Methods), with the exception of geothermal heat flux, which was inferred from crustal thickness (35). This initial heat budget analysis accounts for basal melting of $0.12\text{--}0.30 \text{ mm d}^{-1}$ (Fig. 3b), which is two orders of magnitude lower than the radar-derived BMR (Fig. 1c). Using an enthalpy-based formulation to include additional heat stemming from liquid water in basal ice supplied only another 0.29 W m^{-2} (Fig. 3b; Equations 4 and 5, Methods).

Viscous energy dissipation in the basal drainage system. Our study site is in an area of active subglacial drainage, with delivery of surface meltwater to the glacier bed through supraglacial

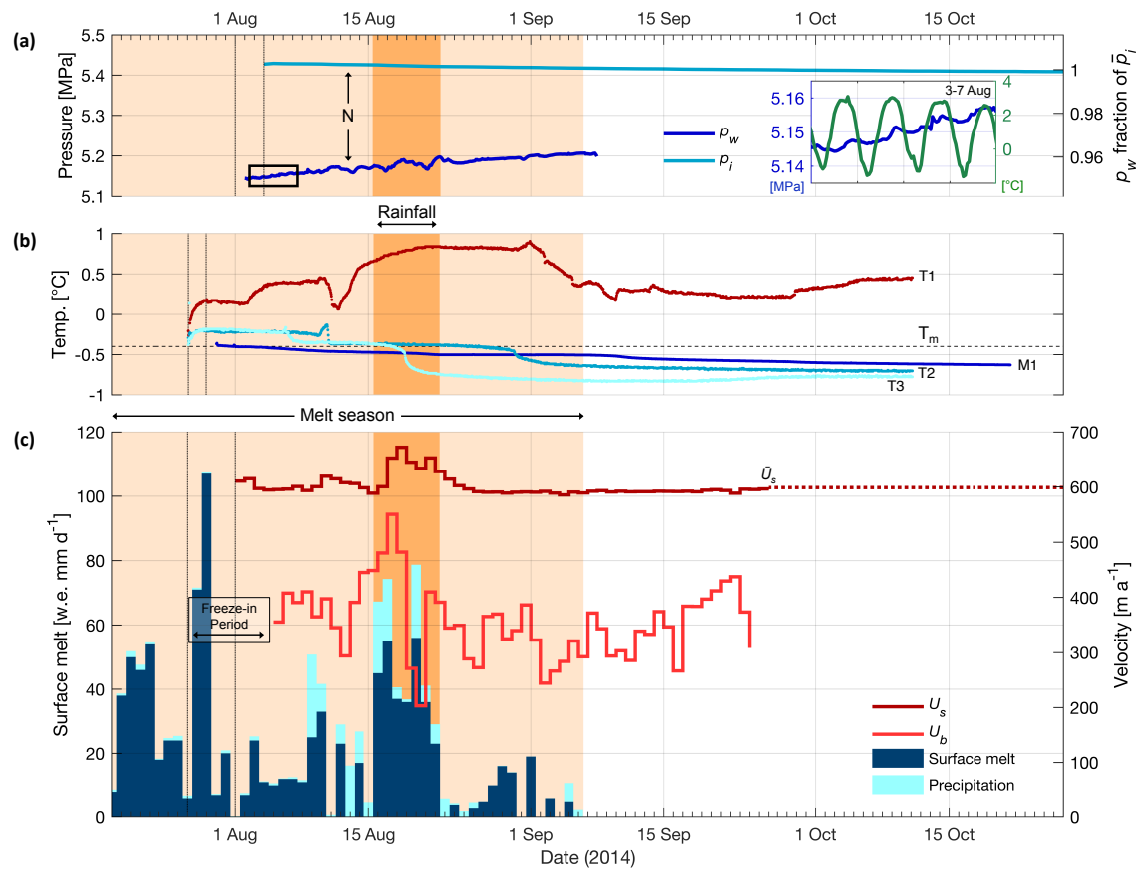


Fig. 2. Borehole records from site S30 on Store Glacier. (a) Basal water pressure (p_w) recorded in a borehole drilled to the bed at site S30. The ice overburden pressure (p_i) is derived from precise co-located ApRES measurements of ice column thickness. The difference between p_i and p_w is the effective pressure (N) used to estimate the basal shear stress and frictional heat produced at the bed. The p_w fraction of overburden pressure (\bar{p}_i) is calculated from the mean radar-derived ice thickness. Vertical grey lines denote approximate time of sensor installation. Inset shows dampened diurnal variations in p_w (blue line) together with strong diurnal fluctuations in surface air temperature (green line), for period marked by black box. (b) Borehole-installed temperature records from hydrological system at thawed glacier bed (T1) and sensors which froze into basal ice immediately above the bed (M1) and approximately 3 m (T2) and 7 m (T3) higher. The horizontal dashed line indicates pressure dependent water-ice phase transition temperature ($T_m = -0.40$ °C). (c) Ice surface velocity (U_s , right axis) recorded from GPS installed at drill site together with rates of basal motion (U_b , right axis) obtained by subtracting ice deformation recorded as tilt in the borehole. \bar{U}_s is the mean ice velocity after the melt season has ended. Stacked bar plot (left axis) shows surface melt recorded by an automatic weather station at the drill site (dark blue) and additional precipitation (light blue) derived from NCEP/NCAR reanalysis data.

lake drainage and hydrofracture resulting in moulines (36). We therefore explored the possibility that the high local basal melt rate is driven by the heat generated by loss of gravitational potential energy as surface meltwater descends to, and flows at, the glacier bed (37). We derived the major drainage paths from hydrologic potential gradients established from surface and bed elevation datasets (38) and calculated the energy balance of surface meltwater traveling beneath the glacier (Equation 2, Methods). In this model, all routed water flows down the hydrologic potential gradient (Equation 3, Methods). As forcing, we used runoff from the RACMO2 regional climate model to prescribe daily inputs of surface water during the 2014 summer melt season (39). With a highly crevassed surface limiting the extent to which meltwater is transported supraglacially (Fig. 1a), we made the simplifying assumptions that surface water reaches the bed in the grid cell it was produced, and that all energy is subsequently dissipated as heat along basal drainage paths. At a spatial resolution of 500 m, we find a close overall agreement between modeled BMR in the central drainage path that passes our study site (S30 on Fig. 3a) and the observed BMR (Fig. 3b). Taking the rainfall

event on 18 August for example (Fig. 4), the model predicts 54 mm of basal melt (Fig. 3a) in the basal drainage path near site S30 compared to the observed 57 mm on that day (Fig. 1c). While model resolution does not change the routing of water according to hydrologic gradients, increasing (decreasing) the resolution will increase (decrease) the modelled BMR because water is routed to smaller (larger) grid cells. The close agreement between our observations and the model at 500 m resolution may reflect the approximate area over which the ice is in contact with flowing water. However, we note that the model is simple and does not feature all of the hydrological processes involved with subglacial drainage. We also cannot rule out that potential energy exchanges during the water's descent to the bed might reduce the energy available for basal melting. If the latter is the case, our model would need a somewhat finer resolution in order to reproduce basal melting at the observed rate. We can nevertheless conclude that the area over which ice is in contact with flowing water at site S30 probably is on the order of some hundreds of metres.

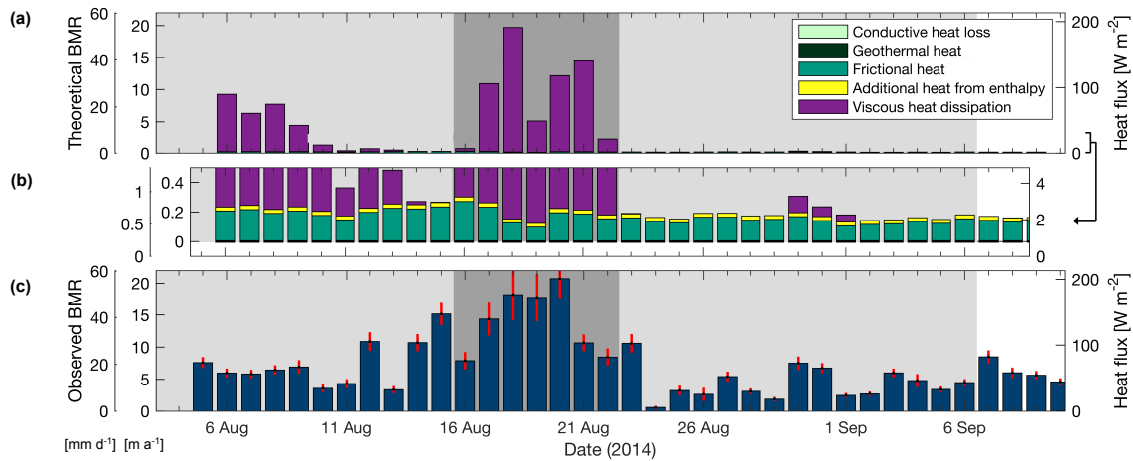


Fig. 3. Sources and sinks of energy and basal melt rate estimates. (a) Theoretical basal melt rates (BMR) at S30 derived from estimates of heat lost by conduction into basal ice and sourced from geothermal heat flux, friction along ice base, enthalpy, and viscous heat dissipation when surface water is routed along the bed. (b) Magnification of (a) to illustrate small magnitude of contributions other than viscous heat dissipation. (c) Corresponding measured basal melt rates from ApRES.

Discussion

The overall agreement between measured and modeled BMR after accounting for viscous heat dissipation show that surface meltwater is a vast, yet over-looked, energy source. While enhanced basal melting from surface meltwater delivered at the bed has previously been inferred from ice-penetrating radar profiles in which internal reflectors dip towards the bed near the injection point (40), our ground-based measurements with ApRES and borehole thermistors provide direct measurements of the process' magnitude and consequent melt rate. A recent large-scale study by Karlsson et al. (41) estimates the GrIS basal ablation to be 5.2 ± 1.6 Gt of ice per year, but notes that the spatial variability in this melting is high and still unconstrained, especially along subglacial drainage pathways where energy from the surface is likely to be focused. Our study resolves this uncertainty by showing that ice melting along basal drainage pathways beneath Store Glacier can reach levels similar to those recorded at the glacier's surface in response to solar heating (Fig. 1c vs. Fig. 2c). This discovery raises important questions concerning viscous dissipation and drainage efficiency. According to the classic theory of water flow in glaciers, flow of water at relatively high pressure in small cavities should be unstable and revert to relatively low pressure flow in channels (42), with channel size reaching a steady state when wall melting by viscous heat dissipation exactly balances creep closure of the conduit (11). Central to this theory are two commonly-used simplifying assumptions, which are: (a) that the temperatures of the water and the ice wall are the same, fixed at the pressure-dependent phase transition temperature; and (b) that heat generated by viscous dissipation is used instantaneously either to melt the conduit walls or to keep the water temperature at the melting point (11). Although the assumed instantaneous heat transfer is practical and widely used (26), there is a physical inconsistency between assuming that the temperature of the water and the ice wall are equal while requiring that viscous heat dissipation in the flowing water leads to the instantaneous melting of those walls. Below, we develop further the implications of this contradiction.

Basal heat transfer. In general, the rate at which heat is exchanged between a solid surface and a liquid flowing in contact with it is proportional to the temperature difference between the two (43). The first order approximation is $Q = h(T_w - T_m)$, where Q is the heat flux, h is the heat transfer coefficient, T_w is the bulk water temperature, and T_m is the pressure-dependent water-ice phase transition temperature of the conduit walls (44). Subglacial water flow can therefore either cause melting of conduit walls or have its bulk temperature equal to the temperature of the walls, but not both at the same time.

The heat transfer responsible for the high BMR we record at Store Glacier can be explained from co-located borehole temperature records at site S30 (30). The lowermost temperature sensor in this borehole record ('T1' in Figure 2) may provide the first clear evidence of viscous heat dissipation in the basal drainage system, where temperatures ranged mostly between 0.2°C and 0.8°C over several months. The peak basal temperature of 0.88°C occurred shortly after the late August rainfall event, which also resulted in a sharp rise in electrical conductivity (30), possibly as a result of ionic enrichment associated with an increased suspended sediment load in the turbulent flow. While the overlying temperature sensors (T2, T3...) froze in and cooled, T1 remained warm and showed no sign of freezing (Fig. 2). The 'warm' T1 record cannot be explained from measurements made below the ice base because the geothermal heat flux is not sufficiently high, nor from mechanical friction alone (Methods). Such warm conditions so close to the ice base contradict the simplifying assumption of instantaneous heat transfer, which dictate that temperatures at the base of ice sheets should be effectively bound by the pressure dependent phase-transition temperature, here -0.40°C . Yet, previous studies have shown that water flowing through a glacier can sustain temperatures well above the freezing point (44–47). Indeed, the equilibrium water temperature reached when viscous heat dissipation in the water equals the heat flux into the surrounding colder ice can match our measured value of 0.88°C in a conduit where the pressure dependent melting point is -0.40°C , e.g. if the hydraulic radius is 2 m and the gradients in local elevation

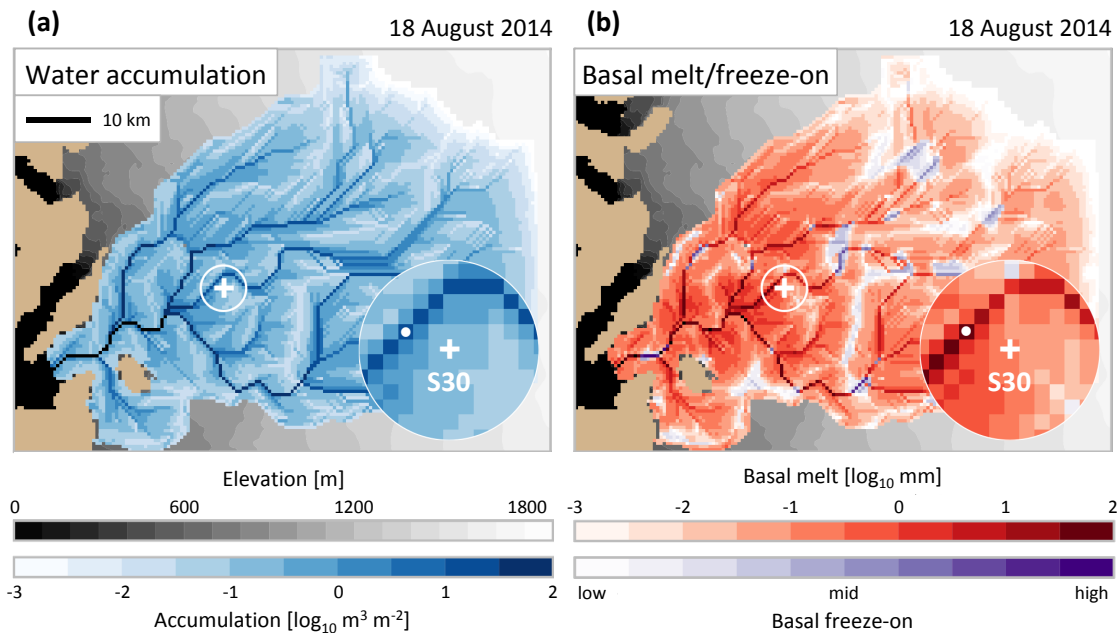


Fig. 4. Basal drainage and viscous heat dissipation. (a) Modeled accumulation of water in the basal drainage system of Store Glacier when hydrologic model transfers RACMO2 surface runoff on 18 August along the bed in the glacier catchment (blue colors). Spatial resolution of model is 500 m. Inset shows water routing near site S30 (+) where ApRES/borehole records were obtained. Grey colors show the ice sheet's surface elevation. (b) Basal melt from modeled viscous heat dissipation in the basal drainage system on 18 August. Red colors denote basal melting and blue colors denote basal freezing, which occurs when energy from viscous dissipation alone cannot raise the temperature of water according to the pressure-dependent phase-transition. Circular inset in (a) shows water accumulating in a major subglacial drainage path (white dot) which passes nearby site S30 (white star). Circular inset in (b) shows corresponding high basal melt rate from viscous heat dissipation.

231 and hydraulic head both reach 5° (Equation 6, Methods).

232 To estimate the heat transfer between the subglacial water
 233 and the basal ice at our study site, we assume that the heat flux
 234 from the highest BMR (57 mm d^{-1}) is provided by the warmest
 235 water ($T_w = 0.88^\circ\text{C}$), and vice versa (i.e. the lowest BMR
 236 of 10 mm d^{-1} for $T_w = 0.19^\circ\text{C}$). This gives a heat transfer
 237 coefficient of approximately $60\text{--}170 \text{ W m}^{-2}\text{ }^\circ\text{C}^{-1}$, which can
 238 be achieved for a large range of water depths of $0.01\text{--}10 \text{ m}$
 239 while the water velocities should be on the order of $1\text{--}10 \text{ cm s}^{-1}$
 240 (Equations 7 and 8, Methods). Our observations also indicate
 241 that heat generated mechanically is advected downstream.
 242 To capture this effect, instantaneous heat transfer cannot be
 243 assumed, and hydrological glacier models will instead need
 244 to solve the energy transport using heat transfer coefficients
 245 that control the rate at which heat generated by mechanical
 246 energy dissipation is transferred to the walls (47). While the
 247 latter was included in original work on Jökulhlaup by Nye (23),
 248 Spring and Hutter (24) and Clarke (25), the energy transport
 249 equation has so far not been implemented widely apart from
 250 the special case of Icelandic outburst floods (23, 48).

251 **Basal drainage.** Our measured BMR indicates that the basal
 252 drainage system would require a dimension at least as large as
 253 the 25 m spatial footprint of the ApRES (Methods). The high
 254 BMR could occur in an efficient system in which channels are
 255 much wider than high (49), or alternatively in a system of
 256 canals (12), which are non-arborescent, but theoretically stable
 257 under ice sheets underlain by sedimentary beds (50). While
 258 channels can also form over sedimentary glacier beds (12), a
 259 system of canals is more consistent with the 45 m-thick layer
 260 of unconsolidated sediments reported at site S30 (31) as well
 261 as high basal water pressures observed close to ($>90\%$) the

ice overburden throughout the period of observation (Fig. 2a).
 However, the high BMR may also occur if a thin film or water
 sheet grows larger than the laminar-turbulent transition and
 is stabilized by clasts protruding into the ice (51). The offset
 between minor diurnal peaks in basal water pressure and the
 daily maximum surface air temperature (Fig. 2) is consistent
 with the latter or canals forming at site S30, while channels
 may develop closer to the terminus (52).

Surface driver of basal melting. The 2014 melt season (1 June
 to 31 August) produced an average of $16 \times 10^6 \text{ m}^3$ of surface
 meltwater per day in the catchment (Fig. S3). Assuming
 that all water drained to the bed, the power for basal melting
 by viscous heat dissipation would range from 0.66 GW on 11
 August when BMR was recorded at 4 mm d^{-1} , to 8.6 GW on
 18 August when the latter was 57 mm d^{-1} (Fig. 1c). The
 recorded peak BMR corresponds with a peak in daily runoff of
 $80 \times 10^6 \text{ m}^3$ (Fig. S3). In comparison, the Three Gorges Dam
 in China produces 0.7 GW of power with a peak flow rate of
 $950 \text{ m}^3 \text{ s}^{-1}$. The average power generated when surface water
 is transferred to the bed at Store Glacier ($\sim 3 \text{ GW}$) dwarfs all
 other basal heat sources. Our observations therefore yield the
 first direct evidence for the sustained impact of the process
 proposed by Mankoff and Tulaczyk (37), who argued that
 present-day runoff on the Greenland Ice Sheet may deliver
 66 GW to its base and that the power available for viscous heat
 dissipation could increase to 110 GW or 320 GW by 2100 under
 IPCC climate scenarios RCP4.5 and RCP8.5 respectively.

Although we have assumed that runoff is directly transferred
 to the bed through the numerous crevasses and moulins
 on Store Glacier (36), analysis of echo strength and attenu-
 ation recorded in our ApRES measurements from site S30

indicates that some of the runoff is instead stored englacially (53). This effect is indirectly included in our study, because the modelled runoff used to quantify viscous dissipation excludes meltwater retention at the surface (39). The latter can be seen in the difference between our measurements of surface ablation and modelled runoff at site S30 (Fig. S2). We also note that the seasonally stored melt volume is a small fraction of the total runoff and that impounded water inferred previously at site S30 has a short (≤ 1 year) residence time (53). However, deep crevasses containing re-frozen meltwater show retention of meltwater to greater depths than previously reported (54). Hence, we cannot rule out the possibility that some of the water we infer to reach the bed may be stored englacially, resulting in a continued delivery of water to the bed after the melt season has ended or cryohydrologic warming in the upper part of the glacier if the water refreezes. The former may explain why the observed BMR remains higher than modelled values when the melt season has ended (Fig. 1), and why oceanographic measurements show a sustained delivery of fresh basal meltwater from Store Glacier into Ikerasak Fjord even in winter (55). Cryohydrologic warming will, however, be important in places where crevasses are deep, but cannot penetrate the full ice thickness (54). The extent to which crevasses will fully or partially penetrate the glacier is controlled by the mean state of stress in the ice which influences the ability of water to pond (56).

The high BMR from ApRES are consistent with theoretical estimates of viscous dissipation in the basal drainage system. They are also supported by independent measurements of warm subglacial water. Our observations therefore call into question the assumption of the thermodynamic equilibrium of water flowing through and beneath glaciers. We have shown that the temperature of meltwater flowing in glacial conduits need not be at the pressure melting point and that heat is not transferred between meltwater and ice instantaneously as assumed by most theoretical studies (11). This means that hydrological glacier models based on Röthlisberger's theory in general may be overestimating rates of conduit enlargement through melting, and, conversely, that viscous dissipation in distributed systems may not result in channel formation even when discharge grows large. This disruption may occur when ice slides rapidly over a rough bed, creating a setting in which protruding sediments or clasts stabilizes a turbulent water sheet (51). Or alternatively if fluvial erosion under the glacier produces a non-arborescent system of canals (50).

Although warming of subglacial water shows that only a portion of the available energy goes into melting, the transfer of water from surface to bed makes channels likely to form near supraglacial lakes, which drain rapidly (36) and form moulins (57) that often continue to deliver large fluxes of water from considerable heights to the glacier bed. While viscous dissipation in that water will promote the growth of channels at these locations in general, a delay between meltwater flux and channel growth may lead to a transfer of water and energy into the enveloping distributed system, creating the conditions we report herein. Numerical modeling of the hydrological system beneath Store Glacier shows that such non-equilibrium conditions are likely to be common (52).

Materials and Methods

The ApRES system. In this study, we deployed an autonomous phase-sensitive radio echo sounder (ApRES) system with 16 cavity-backed bowtie antennas (8 transmitting, 8 receiving) at site S30 on Store Glacier (58). The ApRES recorded the relative depths of internal reflectors and the ice base in a Lagrangian reference frame by transmission of a frequency modulated continuous wave. The signal frequency increases linearly from 200 MHz to 400 MHz over 1 second, corresponding to a (coarse) range resolution of 0.43 m before processing steps (29). Combined with phase measurements embedded within each coarse-range bin, range detection with millimeter precision can be achieved given ideal (low signal-to-noise ratios) conditions (29). The ApRES was deployed to run autonomously, collecting radar reflection data at 4-hourly intervals from 26 July to 4 December 2014, after which the antennas were damaged during strong winds and data collection ceased. The dataset was prepared for calculation of vertical deformation and basal melt rates following well established phase processing procedures (29, 32, 34, 59), as summarized below.

Vertical deformation rates. Every 4 hours, the ApRES system transmitted a burst for each antenna pair, giving a total of 64 chirps per burst (58). The high precision of the system allows the range to englacial reflectors and the ice-bed interface to be resolved at every transmitted burst (Fig. S1a). Vertical ice deformation rates and their respective error were derived for burst pairs separated by 24 hours as shown in Fig. S1b and described in detail by Young et al. (32). For the ApRES data acquired from 26 July to 4 December 2014, we found internal layers vertical displacements to increase linearly through the ice column (Fig. S1d), indicating that the vertical strain rate is depth-independent. We note that only internal layers with a cross-correlation coherence threshold of > 0.925 between consecutive measurements were used to estimate the vertical deformation (32). With this threshold, vertical deformation rates were based on linear displacements of internal layers observed in this upper 80% of the ice column (Fig. S1c). Although we cannot rule out the possibility of a different deformational regime occurring within the lowermost 20% of the ice column, we assume that the strain remained depth-independent throughout the ice column while noting that englacial deformation at depth will typically be either a continuation of the upper (overlying) strain regime or an enhanced expression thereof (32). If the latter were the case, basal melting would be higher than our radar-derived estimates because the ice column is observed to thicken at site S30 (Fig. S1). For the data we present, a robust linear regression model ($R^2 > 0.9$) was the best fit. See Young et al. (32) for details.

Basal melt rates. The basal melt rate was derived from ApRES data using the same approach adopted in studies of Antarctic ice shelves (33, 34). By differencing the total amount of vertical deformation, occurring over the ice column between consecutive measurements, with the concurrent change in ice thickness, we generated a four-month-long time series of daily basal melt rates beneath Store Glacier (Fig. S1). We estimated the total change in ice thickness at each time step by determining the coarse-range offset of the bin enveloping the basal reflector through identifying the amount of lag corresponding to the maximum amplitude of the cross-correlation (Fig. S1e), and its respective fine-range offset through the phase of the complex cross-correlation function (Fig. S1f). The standard error of ice thickness measurements was derived from phase variations across all chirps in each burst, as described by Young et al. (32). The basal melt rate error bounds were calculated as the square root of the sum of the squared errors tied to vertical deformation rate and ice thickness, respectively; thereby taking error propagation into account. The location of the basal reflector was defined as the first range bin in which all bursts coherently capture a single reflector from the dielectric contrast between ice and liquid water at the bed. The shape of the basal reflector within the study area is dictated by the topography of the underlying bed layer, and therefore on a fast-flowing glacier, the aperture footprint of the ApRES array would be incrementally offset due to the down-glacier movement of the ice surface. Range change was therefore conducted incrementally at a time step of 24 h to not only to minimize the change in basal reflector shape but also to enable tracking the basal reflection peak through range and phase. As the radar system is resolution limited with a footprint of radius

426 $\sqrt{2R\Delta R_c}$, where R is the total range from source to reflector and
 427 ΔR_c is the coarse range resolution (0.43 m), this corresponds to a
 428 maximum daily offset in footprint radius and area of 1.8 m (8%) and
 429 167 m^2 (10%) respectively, given the observed maximum surface
 430 velocity of 672 m a^{-1} (Table S2). Because this offset is minor, we
 431 assume no influence on the ApRES measurements. However, we
 432 conservatively apply an additional 10% of the daily measured basal
 433 melt rate values to their respective error bounds in a first attempt
 434 to account for these unknowns.

435 **Basal ice and borehole temperature records.** At the ice-bed inter-
 436 face, the melting-point temperature of ice, adjusted for pressure,
 437 varies according to the Clausius-Clapeyron gradient, which is $C_T =$
 438 $7.42 \times 10^{-8} \text{ }^\circ\text{C MPa}^{-1}$ for pure ice and air free water (Table S1).
 439 With an ice density of 917 kg m^{-3} and a pure ice column with no
 440 firn present, we estimate the pressure-adjusted melting point tem-
 441 perature beneath a nominal 604–606 m of ice to be $T_m = -0.40 \text{ }^\circ\text{C}$.
 442 This melting point temperature is substantially lower than the T1
 443 temperature sensor record used to infer viscous heat dissipation in
 444 the basal drainage system. While we cannot rule out the possibility
 445 of error in our measurements, Doyle et al. (30) show three lines of
 446 evidence that show that the T1 temperature sensor was calibrated
 447 and operational: (i) the thermistor ice bath calibration curve for
 448 T1 was consistent with those of all the other thermistors; (ii) the
 449 temperature time series for T1 does not show the characteristic
 450 freezing curve observed for all the other thermistors, which suggests
 451 that the thermistor did not freeze in; and (iii) damage to the ther-
 452 mistor cable caused by deformation or basal sliding would be likely
 453 to stretch the cables which would increase its resistance and drive
 454 apparent temperature downward, not upward. The observation of
 455 T1 peak temperatures in unison with a spike in electrical conductiv-
 456 ity shortly after the late August rainfall event, which brought warm
 457 air and precipitation over the ice sheet, also indicate that sensor T1
 458 was working (30). During this event, surface ablation was measured
 459 at the seasonal peak rate of 56 mm d^{-1} (30), hence indicating that
 460 the coincident T1 peak was induced by viscous dissipation in an
 461 expanded basal drainage system carrying a large volume of surface
 462 meltwater. Hence, we infer the T1 record to capture water warmed
 463 by viscous heat dissipation in the basal drainage system. The T1
 464 record is in good agreement with, and also independent of, the
 465 radar-derived basal melt rate.

466 **Basal heat budget.** To understand the high basal melt rates observed
 467 beneath Store Glacier we quantified sources and sinks of heat at
 468 the base of the ice sheet:

$$469 \quad G + \tau_b U_b - \theta_b K_i - \dot{m} L \rho_i + Q_{VHD} = 0 \quad [1]$$

470 where G is geothermal heat flux; the second term is frictional heat
 471 calculated from basal shear stress τ_b and basal motion U_b ; the
 472 third term is the conductive heat loss calculated from the basal
 473 ice temperature gradient θ_b and ice thermal conductivity K_i ; the
 474 fourth term is latent heat of fusion calculated from the basal melt
 475 rate \dot{m} (negative when ice base freezes); L is the coefficient of latent
 476 heat of fusion, and ρ_i is the density of ice. The first four terms define
 477 the standard basal heat budget used in most previous work (60) and
 478 is here used in our initial heat budget calculation. The fifth term,
 479 Q_{VHD} , is added in order to also include energy released due to the
 480 viscous resistance in the water flow beneath the ice (37). Below we
 481 describe how each term was quantified.

482 **Geothermal heat flux.** In this study, we used a geothermal heat flux
 483 value of $60 \times 10^{-3} \text{ W m}^{-2}$ based on crustal magnetic field (61)
 484 and thickness (35). Although modeled geothermal heat flux over
 485 Greenland is highly variable, ranging from $40 \times 10^{-3} \text{ W m}^{-2}$ in the
 486 south to $140 \times 10^{-3} \text{ W m}^{-2}$ in the central north where the crust
 487 is thinner, this variability is not important in this study as other
 488 basal heat sources are significantly higher.

489 **Frictional heat.** To quantify the frictional heat, we derived estimates
 490 of the basal shear stress, τ_b , and the rate of basal motion, U_b , from
 491 contemporaneous observations in co-located boreholes. Because the
 492 glacier is underlain by unconsolidated till (31), we used the Coulomb
 493 plastic failure criterion to describe the till's shear strength, i.e. $\tau_b =$
 494 $N \tan(\phi)$, where $N = p_i - p_w$ is the effective pressure calculated
 495 as the difference between ice overburden pressure ($p_i = \rho_i g h_i$),

496 where h_i is the ice thickness measured by ApRES) and the basal
 497 water pressure (p_w , recorded by borehole pressure sensor). Due to
 498 precise measurements of both h_i and p_w (Fig. 2), we were able to
 499 quantify the effective pressure very accurately. The characteristic
 500 friction constant, ϕ , does not vary greatly across different glacial
 501 environments, and we assumed a value of 30° which is shared by
 502 most normally consolidated tills (62). Following Ryser et al. (63),
 503 the rate of basal motion was derived by subtracting tilt recorded in
 504 a borehole drilled to the bed from a contemporaneous GPS record
 505 of surface motion at the borehole site (Fig. 2). The tilt sensors were
 506 processed assuming the produced vertical gradients of horizontal
 507 velocity were all in the flow direction. The resulting time series was
 508 filtered with a two-pole, low-pass Butterworth filter with a 72-hour
 509 cut-off period, and then binned into daily averages to match the
 510 time steps of other parameters. More detailed descriptions of these
 511 borehole records can be found in Doyle et al. (30).

512 **Conductive heat loss.** The conductive heat loss of -60 mW m^{-2}
 513 was derived from the thermal conductivity of ice (Table S1) and a
 514 basal ice temperature gradient of $-0.0286 \text{ }^\circ\text{C m}^{-1}$ established from
 515 borehole temperature records shown in Fig. 2. The equilibrium
 516 temperatures were $-0.86 \text{ }^\circ\text{C}$ for sensor T3 (installed at 596.5 m
 517 below surface), $-0.76 \text{ }^\circ\text{C}$ for sensor T2 (600.5 m) and $-0.64 \text{ }^\circ\text{C}$ for
 518 sensor M1 (603.3 m). Sensor T1 did not freeze in. Details of these
 519 records can be found in Doyle et al. (30).

520 **Viscous heat dissipation.** When surface meltwater is injected to the
 521 bed, energy (Q_{VHD} in Equation 1, Methods) is released due to the
 522 viscous resistance in the water flow. We partitioned this energy into
 523 gravitational and potential energy components, using the approach
 524 described by Mankoff and Tulaczyk (37).

525 Between the injection point and outflow, we assume all energy
 526 is dissipated as heat within the grid cell where the energy transfer
 527 occurs. Henceforth, as water flows down the hydraulic gradient,
 528 we calculate the energy released as heat based on the volume of
 529 water that is routed in each grid cell, including (i) the change in the
 530 hydraulic potential, and (ii) the change in the pressure-dependent
 531 phase transition temperature (37):

$$532 \quad Q_{VHD} = V (\nabla \phi_h - C_T c_p \nabla \phi_{h,p} \rho_w) \quad [2]$$

533 where V is volume of water; $\nabla \phi_h$ is the hydraulic potential gradient,
 534 where the subscript p denotes the pressure component; C_T is the
 535 Clausius-Clapeyron gradient; c_p is the specific heat of water, and
 536 ρ_w is the density of water (see Table S1 for parameter values).

537 **Water routing.** To quantify Q_{VHD} , the amount of energy available
 538 for viscous heat dissipation at site S30, we used a hydrological model
 539 in which water is routed subglacially in the catchment beneath Store
 540 Glacier. Specifically, the model tracks the flux of surface meltwater
 541 from source (i.e. surface runoff reaching the bed) to sink (i.e.
 542 subglacial discharge into fjord), in order to estimate the energy
 543 produced by pressure and elevation changes. The energy for viscous
 544 heat dissipation in the basal drainage system was estimated using
 545 daily values of surface runoff from the RACMO 2.0 regional climate
 546 model (39) under the assumption that all surface water reaches the
 547 bed and that all energy is dissipated as heat (37). To route water,
 548 we used r.watershed tool in GRASS GIS as a directional routing
 549 algorithm in which cells with lower hydraulic potential receive a
 550 fraction of the outflow (37). The hydraulic potential was calculated
 551 as (64):

$$552 \quad \nabla \phi_h = \nabla \phi_{h,z} + \nabla \phi_{h,p} = \rho_w g \nabla z_b + \alpha \rho_i g (\nabla z_s - \nabla z_b) \quad [3]$$

553 where ρ_w is the density of water, g is gravitational acceleration, and
 554 z_b is the bed elevation, prescribed from BedMachine 3.0 topographic
 555 data (38); α is the flotation fraction, here set to 0.9 based on ice
 556 overburden pressure from measured ice thickness and basal water
 557 pressure (Fig. 2); ρ_i is the density of ice, and z_s is the surface
 558 elevation as prescribed by ArcticDEM. The resulting model output
 559 was gridded at a 500 m spatial resolution. Runoff was injected at
 560 the bed beneath the grid cell in which it was produced and the
 561 water was assumed to be at the subglacial pressure-dependent
 562 phase transition temperature, i.e. we ignore any warming at the
 563 surface from radiative sources while assuming that the water cools
 564 according to pressure change between the bed and the surface. The
 565 energy for viscous heat dissipation in our model occurs when there

is a drop in either gravitational potential energy (first term on the RHS in Equation 3) or pressure (second term). When water flows under thinning ice where the phase transition temperature increases, energy is used to warm the water, resulting in either less melting or a switch to basal freezing if the drop in gravitational potential energy cannot provide sufficient heat. Basal freezing may also occur if water flows uphill and the pressure drop cannot provide sufficient energy, whereas viscous heat dissipation will melt ice the fastest when there is a drop in gravitational potential and an increase in pressure.

Enthalpy of basal ice. To supplement the thermomechanical model (Equation 1), we also calculated basal melting under the assumption that the basal ice is at the phase change temperature. In this case, we used a 1-dimensional representation of the jump equation for enthalpy to derive a basal melt rate (9):

$$\dot{m}_b = \frac{\tau_b \dot{U}_b + G + q_{i_e} - \rho_w \eta_b \gamma (dp_w/dt)}{H - H_l(p_w)} \quad [4]$$

The first and second terms on the RHS of Equation 4 are the frictional heat and geothermal heat flux (described above). The last term expresses the effect from changes in subglacial water pressure, p_w , where $\gamma (dp_w/dt)$ and $H_l(p_w)$ is the enthalpy of the liquid water, and η_b represent the thickness of the subglacial water layer. The third term, q_{i_e} , is the non-advective heat flux into temperate basal ice expressed in terms of pressure (p) and enthalpy (H):

$$q_{i_e} = - (k \nabla T_m(p) + K_0 \nabla H) \quad [5]$$

where $k(H, p) = (1 - \omega_w(H, p)) k_i(H) + \omega_w(H, p) k_w$ is the thermal conductivity of the temperate ice-water mixture, with k_i for pure ice and k_w for liquid water, ω_w is the water fraction, and K_0 is temperate ice diffusivity. Figure 3 shows the additional energy for basal melting, when melt rates from Equation 4 based on parameter values shown in Table S1 are compared with those derived from Equation 1.

Equilibrium water temperature. Energy dissipation occurs inside glacial conduits due to viscous resistance in the flow. As the dissipating energy warms the water (see main text), the heat loss into the conduit ice wall also grows, which gives an equilibrium condition when the two are equal. In a straight inclined conduit with stable water flow, the equilibrium temperature is (44):

$$T_\infty = T_m + \frac{g \cdot \rho_w \cdot R \cdot s}{c} \quad [6]$$

where R is hydraulic radii; s is the hydraulic slope based which combines the gradients of elevation and pressure head, and c is an empirical constant for turbulent flow at 0 °C (see Table S1 for value). Equation 6 shows that T_∞ will always be higher than T_m and that water temperature of 0.88 °C can be reached when T_m is -0.40 °C, e.g. if the gradients of elevation and pressure head are 5° each and R is 2 m.

Heat transfer. We estimated the heat transfer to be 60–170 W m⁻² °C⁻¹ by assuming that the highest (lowest) observed basal melt rates of 57 mm d⁻¹ (10 mm d⁻¹) were driven by water temperatures measured at 0.88 °C (0.19 °C). To make a first order estimate of the associated water flow rate, v , we assumed a linear relationship with the heat transfer coefficient (44):

$$v = h/c \quad [7]$$

where c is the constant for turbulent flow at 0 °C (Table S1). The observationally derived heat transfer of 60–170 W m⁻² °C⁻¹ can therefore be associated with theoretical flow velocities of 2.2–6.6 cm s⁻¹.

To link the heat transfer with a first order estimate of the water depth, D , we turned to an empirical relationship developed for heat transfer to a river ice cover (65):

$$h = B \cdot (v^{0.8}/D^{0.2}) \quad [8]$$

where B is an empirical constant (Table S1). This equation suggests that the heat transfer coefficient is relatively insensitive to the water depth and that the main control comes from flow velocity. A heat transfer coefficient of 60–170 W m⁻² °C⁻¹ can be achieved for a

large range of water depths between 0.01–10 m, while the water velocities should be on the order of 1–10 cm s⁻¹.

ACKNOWLEDGMENTS. The authors are grateful to Ann Andreasen and the Uummannaq Polar Institute for their generous support and hospitality. The authors also wish to thank Sam Doyle for his insightful comments on earlier drafts of this manuscript.

1. J Weertman, On the sliding of glaciers. *J. Glaciol.* **3**, 33–38 (1957).
2. B Kamb, Sliding motion of glaciers: Theory and observation. *Rev. Geophys.* **8**, 673–728 (1970).
3. JF Nye, Glacier sliding without cavitation in a linear viscous approximation. *Proc. Royal Soc. Lond. A: Math. Phys. Eng. Sci.* **315**, 381–403 (1970).
4. L Liboutry, General Theory of Subglacial Cavitation and Sliding of Temperate Glaciers. *J. Glaciol.* **7**, 21–58 (1968).
5. A Iken, The Effect of the Subglacial Water Pressure on the Sliding Velocity of a Glacier in an Idealized Numerical Model. *J. Glaciol.* **27**, 407–421 (1981).
6. WB Kamb, Rheological nonlinearity and flow instability in the deforming bed mechanism of ice stream motion. *J. Geophys. Res. Solid Earth* **96**, 16585–16595 (1991).
7. Engelhardt, Hermann F., WB Kamb, Basal sliding of Ice Stream B, West Antarctica. *J. Glaciol.* **44**, 223–230 (1998).
8. JA MacGregor, et al., A synthesis of the basal thermal state of the Greenland Ice Sheet. *J. Geophys. Res. Earth Surf.* **121**, 1328–1350 (2016).
9. A Aschwanden, E Bueler, C Khroulev, H Blatter, An enthalpy formulation for glaciers and ice sheets. *J. Glaciol.* **58**, 441–457 (2012).
10. CG Schoof, Ice-sheet acceleration driven by melt supply variability. *Nature* **468**, 803–806 (2010).
11. H Röthlisberger, Water pressure in intra-and subglacial channels. *J. Glaciol.* **11**, 177–203 (1972).
12. JS Walder, A Fowler, Channelized subglacial drainage over a deformable bed. *J. Glaciol.* **40**, 3–15 (1994).
13. B Kamb, Glacier surge mechanism based on linked cavity configuration of the basal water conduit system. *J. Geophys. Res. Solid Earth* **92**, 9083–9100 (1987).
14. J Weertman, General theory of water flow at the base of a glacier or ice sheet. *Rev. Geophys.* **10**, 287–333 (1972).
15. GE Flowers, Hydrology and the future of the Greenland Ice Sheet. *Nat. communications* **9**, 1–4 (2018).
16. DM Chandler, et al., Evolution of the subglacial drainage system beneath the Greenland Ice Sheet revealed by tracers. *Nat. Geosci.* **6**, 195–198 (2013).
17. BJ Davison, et al., Subglacial Drainage Evolution Modulates Seasonal Ice Flow Variability of Three Tidewater Glaciers in Southwest Greenland. *J. Geophys. Res. Earth Surf.* **125** (2020).
18. T Moon, et al., Distinct patterns of seasonal Greenland glacier velocity. *Geophys. Res. Lett.* **41**, 7209–7216 (2014).
19. E Rignot, J Mougnot, Ice flow in Greenland for the international polar year 2008–2009. *Geophys. Res. Lett.* **39**, 1–7 (2012).
20. A Aschwanden, et al., Contribution of the Greenland Ice Sheet to sea level over the next millennium. *Sci. Adv.* **5** (2019).
21. GA Catania, LA Stearns, TA Moon, EM Enderlin, RH Jackson, Future Evolution of Greenland's Marine-Terminating Outlet Glaciers. *J. Geophys. Res. Earth Surf.* **125**, 1–28 (2020).
22. JS Walder, Stability of sheet flow of water beneath temperate glaciers and implications for glacier surging. *J. Glaciol.* **28**, 273–293 (1982).
23. JF Nye, Water Flow in Glaciers: Jökulhlaups, Tunnels and Veins. *J. Glaciol.* **17**, 181–207 (1976).
24. U Spring, K Hutter, Numerical studies of Jökulhlaups. *Cold Reg. Sci. Technol.* **4**, 227–244 (1981).
25. GKC Clarke, Hydraulics of subglacial outburst floods: New insights from the Spring–Hutter formulation. *J. Glaciol.* **49**, 299–313 (2003).
26. JS Walder, Röthlisberger channel theory: its origins and consequences. *J. Glaciol.* **56**, 1079–1086 (2010).
27. M Fahnestock, W Abdalati, IP Joughin, J Brozna, P Gogineni, High Geothermal Heat Flow, Basal Melt, and the Origin of Rapid Ice Flow in Central Greenland. *Science* **294**, 2338–2342 (2001).
28. O Zeising, A Humbert, Indication of high basal melting at EastGRIP drill site on the Northeast Greenland Ice Stream. *The Cryosphere Discuss.* **2021**, 1–15 (2021).
29. PV Brennan, LB Lok, K Nicholls, H Corr, Phase-sensitive FMCW radar system for high-precision Antarctic ice shelf profile monitoring. *IET Radar, Sonar & Navig.* **8**, 776–786 (2014).
30. SH Doyle, et al., Physical Conditions of Fast Glacier Flow: 1. Measurements From Boreholes Drilled to the Bed of Store Glacier, West Greenland. *J. Geophys. Res. Earth Surf.* **123**, 324–348 (2018).
31. C Hofstede, et al., Physical Conditions of Fast Glacier Flow: 2. Variable Extent of Anisotropic Ice and Soft Basal Sediment From Seismic Reflection Data Acquired on Store Glacier, West Greenland. *J. Geophys. Res. Earth Surf.* **123**, 349–362 (2018).
32. TJ Young, et al., Physical Conditions of Fast Glacier Flow: 3. Seasonally-Evolving Ice Deformation on Store Glacier, West Greenland. *J. Geophys. Res. Earth Surf.* **124**, 245–267 (2019).
33. CL Stewart, P Christoffersen, KW Nicholls, MJM Williams, JA Dowdeswell, Basal melting of Ross Ice Shelf from solar heat absorption in an ice-front polynya. *Nat. Geosci.* **12**, 435–440 (2019).
34. I Vaňková, et al., Observations of tidal melt and vertical strain at the Filchner-Ronne Ice Shelf, Antarctica. *J. Geophys. Res. Earth Surf.* **125**, e2019JF005280 (2020).
35. AG Petrunin, et al., Heat flux variations beneath central Greenland's ice due to anomalously thin lithosphere. *Nat. Geosci.* **6**, 746–750 (2013).

- 709 36. TR Chudley, et al., Supraglacial lake drainage at a fast-flowing Greenlandic outlet glacier.
710 *Proc. Natl. Acad. Sci. United States Am.* **116**, 25468–25477 (2019).
- 711 37. KD Mankoff, SM Tulaczyk, The past, present, and future viscous heat dissipation available
712 for Greenland subglacial conduit formation. *The Cryosphere* **11**, 303–317 (2017).
- 713 38. M Moriglihem, et al., BedMachine v3: Complete bed topography and ocean bathymetry map-
714 ping of Greenland from multibeam echo sounding combined with mass conservation. *Geo-
715 physics. research letters* **44**, 11–51 (2017).
- 716 39. B Noël, et al., Modelling the climate and surface mass balance of polar ice sheets using
717 RACMO2-Part 1: Greenland (1958-2016). *Cryosphere* **12**, 811–831 (2018).
- 718 40. G Catania, C Hulbe, H Conway, Grounding-line basal melt rates determined using radar-
719 derived internal stratigraphy. *J. Glaciol.* **56**, 545–554 (2010).
- 720 41. NB Karlsson, et al., A first constraint on basal melt-water production of the Greenland ice
721 sheet. *Nat. Commun.* **12**, 3461 (2021).
- 722 42. JS Walder, Hydraulics of subglacial cavities. *J. Glaciol.* **32**, 439–445 (1986).
- 723 43. L Prandtl, *Essentials of fluid dynamics: with applications to hydraulics, aeronautics, meteoro-
724 logic and other subjects.* (Blackie & Son), (1953).
- 725 44. E Isenko, R Naruse, B Mavlyudov, Water temperature in englacial and supraglacial channels:
726 Change along the flow and contribution to ice melting on the channel wall. *Cold regions
727 science technology* **42**, 53–62 (2005).
- 728 45. R Hock, RL Hooke, Evolution of the internal drainage system in the lower part of the ablation
729 area of Storglaciären, Sweden. *Geol. Soc. Am. Bull.* **105**, 537–546 (1993).
- 730 46. T Jóhannesson, T Thorsteinsson, A Stefánsson, EJ Gaidos, B Einarsson, Circulation and
731 thermodynamics in a subglacial geothermal lake under the Western Skaftá cauldron of the
732 Vatnajökull ice cap, Iceland. *Geophys. research letters* **34** (2007).
- 733 47. AN Sommers, H Rajaram, Energy Transfer by Turbulent Dissipation in Glacial Conduits. *J.
734 Geophys. Res. Earth Surf.* **125**, 1–18 (2020).
- 735 48. GKC Clarke, Glacier outburst floods from Hazard Lake, Yukon Territory, and the problem of
736 flood magnitude prediction. *J. Glaciol.* **28**, 3–21 (1982).
- 737 49. PM Cutler, Modelling the evolution of subglacial tunnels due to varying water input. *J. Glaciol.*
738 **44**, 485–497 (1998).
- 739 50. FSL Ng, Canals under sediment-based ice sheets. *Annals Glaciol.* **30**, 146–152 (2000).
- 740 51. TT Creyts, CG Schoof, Drainage through subglacial water sheets. *J. Geophys. Res. Earth
741 Surf.* **114** (2009).
- 742 52. SJ Cook, P Christoffersen, J Todd, D Slater, N Chauché, Coupled modelling of subglacial
743 hydrology and calving-front melting at Store Glacier, West Greenland. *The Cryosphere* **14**,
744 905–924 (2020).
- 745 53. AK Kendrick, et al., Surface Meltwater Impounded by Seasonal Englacial Storage in West
746 Greenland. *Geophys. Res. Lett.* **45**, 10,474–10,481 (2018).
- 747 54. B Hubbard, et al., Borehole-based characterization of deep mixed-mode crevasses at a
748 greenlandic outlet glacier. *AGU Adv.* **2**, e2020AV000291 (2021).
- 749 55. N Chauché, Ph.D. thesis (Aberystwyth University) (2016).
- 750 56. TR Chudley, et al., Controls on water storage and drainage in crevasses on the greenland ice
751 sheet. *J. Geophys. Res. Earth Surf.* **126**, e2021JF006287 (2021).
- 752 57. A Banwell, I Hewitt, I Willis, N Arnold, Moulin density controls drainage development beneath
753 the Greenland Ice Sheet. *J. Geophys. Res. Earth Surf.* **121**, 2248–2269 (2016).
- 754 58. TJ Young, et al., Resolving the internal and basal geometry of ice masses using imaging
755 phase-sensitive radar. *J. Glaciol.* **64**, 649–660 (2018).
- 756 59. KW Nicholls, et al., Instruments and methods: A ground-based radar for measuring vertical
757 strain rates and time-varying basal melt rates in ice sheets and shelves. *J. Glaciol.* **61**, 1079–
758 1087 (2015).
- 759 60. K Cuffey, WS Paterson, *The Physics of Glaciers.* (Academic Press, Amsterdam), 4 edition, p.
760 704 (2010).
- 761 61. C Fox Maule, ME Purucker, N Olsen, Inferring magnetic crustal thickness and geothermal
762 heat flux from crustal magnetic field models, (Danish Meteorological Institute), Technical re-
763 port (2009).
- 764 62. T Murray, Assessing the paradigm shift: Deformable glacier beds. *Quat. Sci. Rev.* **16**, 995–
765 1016 (1997).
- 766 63. C Rysner, et al., Caterpillar-like ice motion in the ablation zone of the Greenland ice sheet. *J.
767 Geophys. Res. Earth Surf.* **119**, 2258–2271 (2014).
- 768 64. RL Shreve, Movement of water in glaciers. *J. Glaciol.* **11**, 205–214 (1972).
- 769 65. GD Ashton, The presence of ice on rivers changes their behavior, interferes with their use,
770 and causes severe economic disruption. *Am. Sci.* **67**, 38–45 (1979).